



Tensile properties and strengthening mechanisms of eutectic high-entropy alloys induced by heterostructure

Xu Yang, Li Feng, Tong Liu, Ruirun Chen^{*}, Gang Qin, Shiping Wu

National Key Laboratory for Precision Hot Processing of Metals, Harbin Institute of Technology, 150001, PR China



ARTICLE INFO

Keywords:

Eutectic high entropy alloy
Heterostructure
Tensile properties
Strengthening mechanism

ABSTRACT

To investigate the strengthening and deformation behavior of heterogeneous dual-phase high-entropy alloys (HEAs), $\text{Al}_x\text{CoCrFeNi}_3$ ($x = 1, 1.1, 1.15, 1.2, 1.25$ and 1.3) HEAs were designed and prepared. The microstructure consists of FCC phase rich in Co-Cr-Fe-Ni and BCC phase rich in Ni-Al, forming a soft and hard heterostructure. With the increase of Al, the microstructure changes from hypoeutectic to hypereutectic, and $\text{Al}_{1.25}\text{CoCrFeNi}_3$ alloy exhibits a fine eutectic lamellar morphology. Tensile results show that the strength of $\text{Al}_x\text{CoCrFeNi}_3$ HEAs tends to increase and then decrease with increasing Al elements. $\text{Al}_{1.25}\text{CoCrFeNi}_3$ alloy achieves the highest yield strength (535.32 MPa) and tensile strength (1060.59 MPa) as well as high plasticity (17.21%), achieving a balance of strength and plasticity. Interfacial strengthening, grain boundary strengthening, solid solution strengthening and friction stress strengthening play an important role. During the tensile process, the eutectic lamellar heterostructure results in long-range back stress, which induces the high strain hardening ability of FCC phase. Due to the continuous transformation of stress in lamellar heterostructure, the cracks initiate in BCC phase and passivate in FCC phase, which forms synergistic strengthening effects.

1. Introduction

High entropy alloys (HEAs), first proposed by Cantor and Yeh in 2004, have attracted much attention from scholars due to their different microstructure and mechanical properties from traditional alloys [1,2]. HEAs composed of multi-principal elements have high entropy, lattice distortion, hysteresis diffusion and cocktail effects [3–7]. Due to the unique properties and interactions of multiple elements, HEAs have excellent mechanical properties, like wear resistance, corrosion resistance and radiation resistance [8–12]. HEAs with high mixed entropy generally form a simple solid solution structure, such as the most widely studied face-centered cubic (FCC) HEAs and body-centered cubic (BCC) HEAs. However, FCC HEAs have excellent plasticity, but poor strength, and BCC HEAs have high strength but poor plasticity [13–16]. Single-phase HEAs are difficult to achieve the balance of strength and plasticity, which limits the development of industrial applications.

In order to comprehensively improve the plasticity and strength of HEAs, Lu et al. proposed the concept of eutectic high-entropy alloys (EHEAs) in 2014 by referring to the definition of traditional eutectic alloys [17]. EHEAs are generally composed of soft and hard phases, overcoming the strength-ductility trade-off [18,19]. In addition, EHEAs

have the inherent advantages of traditional eutectic alloys, such as low melting temperatures, good fluidity, excellent casting performance, fewer casting defects and in-situ self-generated structure, and have broad industrial application prospects [20–24].

At present, the mechanical properties of EHEAs mainly depend on the phase composition. EHEAs with BCC/B2 structure and BCC/intermetallic compound structure have excellent strength, but both phases are hard phases, resulting in poor plasticity [25,26]. In contrast, EHEAs with FCC/BCC structures can achieve a synergistic strengthening effect while ensuring plasticity due to the alternating distribution of soft and hard phases and achieve a balance between strength and plasticity. Wu et al. developed a series of Al-Co-Cr-Fe-Ni EHEAs through new strategies such as machine learning, which achieved the combination of strength and plasticity [27,28]. Mao et al. prepared a series of BCC/FCC EHEAs such as $\text{Al}_{0.83}\text{Cr}_{0.6}\text{Fe}_{1.4}\text{Ni}_{2.17}$ and $\text{Al}_{0.85}\text{Cr}_{0.4}\text{Fe}_{1.6}\text{Ni}_{2.15}$. FCC phase in the alloy occupies a large proportion (more than 63%), resulting in excellent plasticity and relatively high strength [19]. Shi et al. prepared $\text{Fe}_{20}\text{Co}_{20}\text{Ni}_{41}\text{Al}_{19}$ BCC/FCC ultrafine lamellar EHEA, forming sustained and effective strain-hardening capability, and obtaining special ductility with high tensile strength [29]. Chung et al. developed a series of $\text{Al}_{(18-2x)}\text{Co}_{30}\text{Cr}_{(11+x)}\text{Fe}_{(11+x)}\text{Ni}_{30}$ eutectic and near-eutectic FCC/BCC HEAs,

* Corresponding author.

E-mail address: ruirunchen@hit.edu.cn (R. Chen).

which have superior fracture toughness. This synergistic enhancement of strength and toughness is mainly due to the high heterogeneity deformation induced strengthening/toughening of the phase interface [30]. Wu et al. designed $\text{Ni}_{30}\text{Co}_{30}\text{Cr}_{10}\text{Fe}_{10}\text{Al}_{18}\text{W}_2$ and $\text{Co}_{30}\text{Cr}_{10}\text{Fe}_{10}\text{Al}_{18}\text{Ni}_{32-x}\text{Mo}_x$ EHEAs by adding a small amount of W and Mo elements to Al-Co-Cr-Fe-Ni alloys, and further improved the properties by alloying and recrystallization [31–33]. It can be found that the key to improving the properties of EHEAs is to regulate the ratio of the soft and hard phases. In previous studies, the phase ratio of BCC is reduced in order to ensure the plasticity of the alloy, resulting in a reduction in strength. Moreover, the mechanisms of strengthening and deformation formed by the interaction between heterogeneous structures have been little studied.

Previous studies have shown that AlCoCrFeNi_3 HEAs have a hypoeutectic structure with FCC as the primary phase and have excellent plasticity [34–36]. Therefore, based on the previous work, this work increased the content of Al and designed dual-phase $\text{Al}_x\text{CoCrFeNi}_3$ HEAs with high BCC phase content to improve strength. The microstructure and mechanical properties were systematically studied to reveal the interactions between heterogeneous structures and further develop the relationship between microstructure and micromechanical behavior.

2. Experimental Procedure

$\text{Al}_x\text{CoCrFeNi}_3$ ($x = 1, 1.1, 1.15, 1.2, 1.25$ and 1.3 , simplified as $\text{Al}_1, \text{Al}_{1.1}, \text{Al}_{1.15}, \text{Al}_{1.2}, \text{Al}_{1.25}$ and $\text{Al}_{1.3}$) HEAs were prepared by vacuum arc-melting furnaces under a high purity argon atmosphere, using the constituent elements with a purity higher than 99.5%. Each ingot was repeatedly melted six times to ensure a homogeneous composition. Both microstructure observation specimens and tensile specimens were obtained from ingots by spark machining.

Phase composition was detected by X-ray diffraction (XRD, MXP21V AHF) using Cu K α radiation in the range 20° – 100° at a rate of $8^\circ/\text{min}$. Microstructure was observed using the scanning electron microscope (SEM, TM4000). The energy-dispersive spectrometer (EDS, Q75) was used to analyse the elemental distribution. The microstructure and strain of the specimens after fracture were analyzed by electron back-scattered diffraction (EBSD, Zeiss Super55). The actual composition was

measured by inductively coupled plasma spectrometer (ICP, ICP 7400). The high temperature differential scanning calorimeter (DSC, STA 449 F3) was used for thermal analysis at a heating rate of $10 \text{ K}/\text{min}$.

The gauge length of the tensile specimen is 15 mm , the thickness is 1.8 mm , and the width is 2 mm . Tensile properties were measured using an Instron 5569 universal tensile testing machine at a rate of $1 \text{ mm}/\text{min}$ and three specimens of each alloy were tested to ensure the accuracy of the data. The hardness values and parameters of the phases were determined using G200 nanoindentation with a maximum depth of 300 nm .

3. Results

3.1. Phase Composition and Microstructure

The XRD patterns of the $\text{Al}_x\text{CoCrFeNi}_3$ HEAs are shown in Fig. 1(a), all the alloys are composed of FCC and BCC phases. It can be seen from the enlarged diagram (Fig. 1(b)) of the (111) FCC diffraction peak that as the Al element increases, the (111) FCC diffraction peak shifts toward a lower reflection angle. With the increase of Al element, the content of Al atoms with large radius dissolved into FCC phase increases, causing lattice distortion and increasing lattice constant.

The microstructure and elemental distribution of $\text{Al}_x\text{CoCrFeNi}_3$ HEAs are displayed in Fig. 2. $\text{Al}_1, \text{Al}_{1.1}$ and $\text{Al}_{1.15}$ alloys show obvious hypoeutectic structures in Fig. 2(a–c). FCC phase with dendritic morphology is the primary phase, and the BCC/FCC eutectic lamellar is formed between the dendrites. $\text{Al}_{1.2}$ and $\text{Al}_{1.25}$ alloys are composed of eutectic lamellar structure, divided into regular eutectic and irregular eutectic morphology in Fig. 2(d–e). In each grain, the irregular lamellae are epitaxially grown from the regularly arranged lamellar eutectic structure at the center. When the two grains meet, the irregular eutectic becomes coarser. Comparing the lamellar thickness ($(\lambda_{\text{FCC}} + \lambda_{\text{BCC}})/2$) of the two alloys, the regular eutectic lamellar thickness of $\text{Al}_{1.25}$ alloy is $2.41 \mu\text{m}$, which is smaller than that of $\text{Al}_{1.2}$ alloy ($4.51 \mu\text{m}$). $\text{Al}_{1.3}$ alloy exhibits a hypereutectic structure, and the primary phase transforms into a dendritic BCC phase, as shown in Fig. 2(f). As Al increases, the content of BCC phase increases from 11.85% (Al_1 alloy, as shown in Fig. 2(a)) to 44.98% ($\text{Al}_{1.3}$ alloy, as shown in Fig. 2(f)) and FCC phase

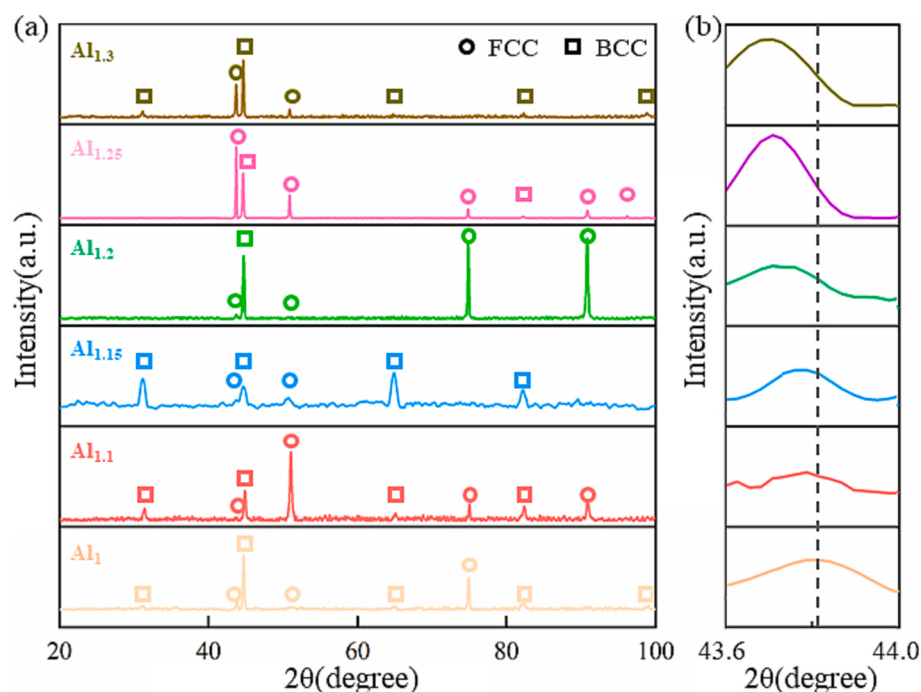


Fig. 1. XRD patterns of $\text{Al}_x\text{CoCrFeNi}_3$ HEAs: (a) XRD patterns; (b) The enlarged views of (111) FCC diffraction peak.

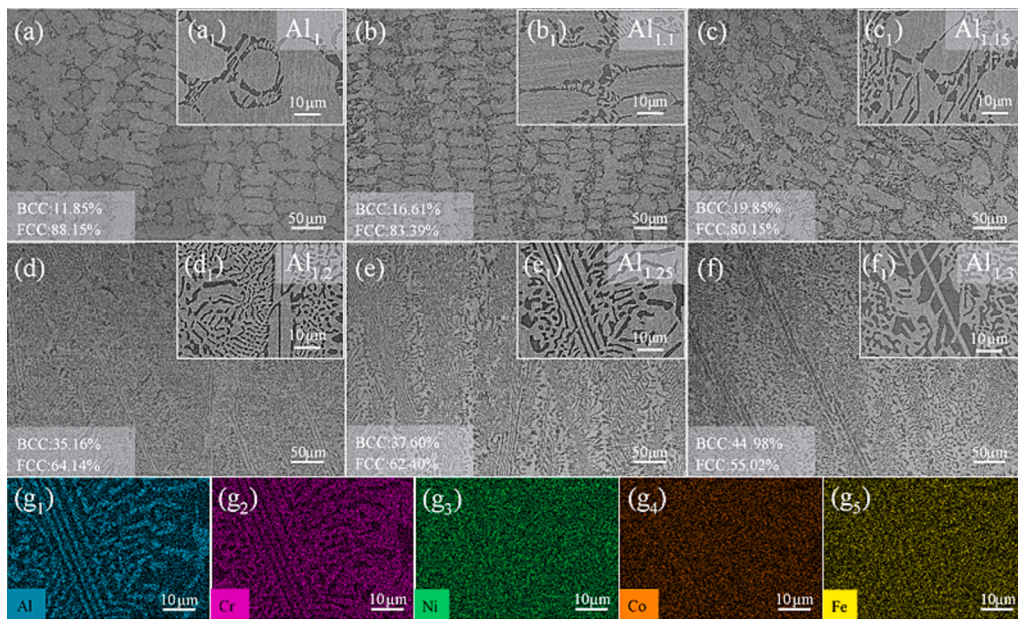


Fig. 2. Microstructure and element distribution of $\text{Al}_x\text{CoCrFeNi}_3$ HEAs: (a-f) Microstructure of $\text{Al}_x\text{CoCrFeNi}_3$ HEAs; (g) Element distribution diagram of $\text{Al}_{1.25}$ alloy.

decreases from 88.15% to 55.02%.

Fig. 2(g) shows the element distribution of $\text{Al}_{1.25}$ alloy, and it can be seen that the elements have obvious segregation. The contents of different elements are analyzed in detail. The nominal compositions of $\text{Al}_{1.25}$ alloy, the actual compositions (measured by ICP) and the elemental contents of the two phases are shown in Table 1. Compared with the nominal composition, FCC phase is rich in Co, Cr, Fe and Ni and lean in Al, while BCC phase is enriched in Ni and Al and depleted of Co, Cr and Fe. Combined with XRD results, it can be inferred that $\text{Al}_{1.25}$ alloy is composed of FCC phase rich in Co-Cr-Fe-Ni and BCC phase rich in Ni-Al.

In order to explore the phase structure of $\text{Al}_{1.25}$ alloy with a fine lamellar eutectic structure and further explain the phase transition, a DSC test was carried out (as shown in Fig. 3). There is only one sharp peak in the curve, proving that there is only one phase transformation process during the heating process. The results are consistent with the characteristics of eutectic reaction, which proves that $\text{Al}_{1.25}$ alloy is EHEA.

3.2. Mechanical Properties

Engineering stress-strain curve of $\text{Al}_x\text{CoCrFeNi}_3$ HEAs is shown in Fig. 4(a). The curves of tensile strength, yield strength and fracture strain with the increase of Al content are shown in Fig. 4(b-d). The tensile strength and yield strength of $\text{Al}_x\text{CoCrFeNi}_3$ HEAs increase first and then decrease with the increase in Al. The strength of $\text{Al}_{1.25}$ alloy is the highest, which may be related to the fine eutectic lamellar structure. The fine eutectic structure increases the proportion of phase boundaries and increases the contribution of interfacial strengthening. The fracture strain gradually decreases with the increase of Al (as shown in Fig. 4(d)), which attributes to the increase of the content of the hard and brittle

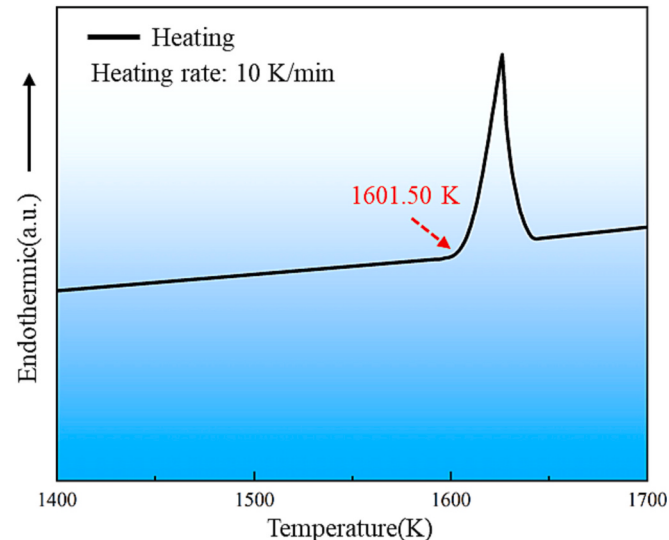


Fig. 3. DSC curve of $\text{Al}_{1.25}$ alloy.

BCC phase. Table 2 shows the properties of $\text{Al}_x\text{CoCrFeNi}_3$ HEAs. Al_1 alloy has the highest fracture strain (31.16%) and the lowest yield strength (447.77 MPa), which is due to the highest proportion of FCC phase. $\text{Al}_{1.25}$ alloy has the highest yield strength (535.32 MPa) and tensile strength (1060.59 MPa) and a relatively high fracture strain (17.21%), achieving an excellent balance of strength and plasticity.

Fig. 5 shows the comparison of the yield strength and fracture strain of $\text{Al}_{1.25}$ alloy with other AlCoCrFeNi eutectic and near-eutectic HEAs, showing that $\text{Al}_{1.25}$ alloy achieves an excellent balance of strength and plasticity [18,19,22,27,29–46]. AlCoCrFeNi HEAs in this work and the previous work are composed of FCC and BCC phases, but the difference in relative content seriously affects the balance of strength and plasticity. Excessive FCC increases the plasticity but decreases the strength, and conversely, increases the strength but decreases the plasticity. In this work, the matrix with a relatively high Ni content was designed, and $\text{Al}_{1.25}$ alloy with high strength and plasticity was prepared by adjusting the content of Al.

Fig. 6 shows the fracture morphologies of $\text{Al}_x\text{CoCrFeNi}_3$ HEAs. All

Table 1

Chemical composition (at.%) of $\text{Al}_{1.25}\text{CoCrFeNi}_3$ alloy.

	Elements (at.%)				
	Al	Co	Cr	Fe	Ni
Nominal composition	17.2	13.8	13.8	13.8	41.4
Actual composition	16.93	16.00	15.59	13.80	37.68
FCC	11.6	16.5	16.2	16.5	39.2
BCC	29.6	10.7	6.5	9.0	44.2

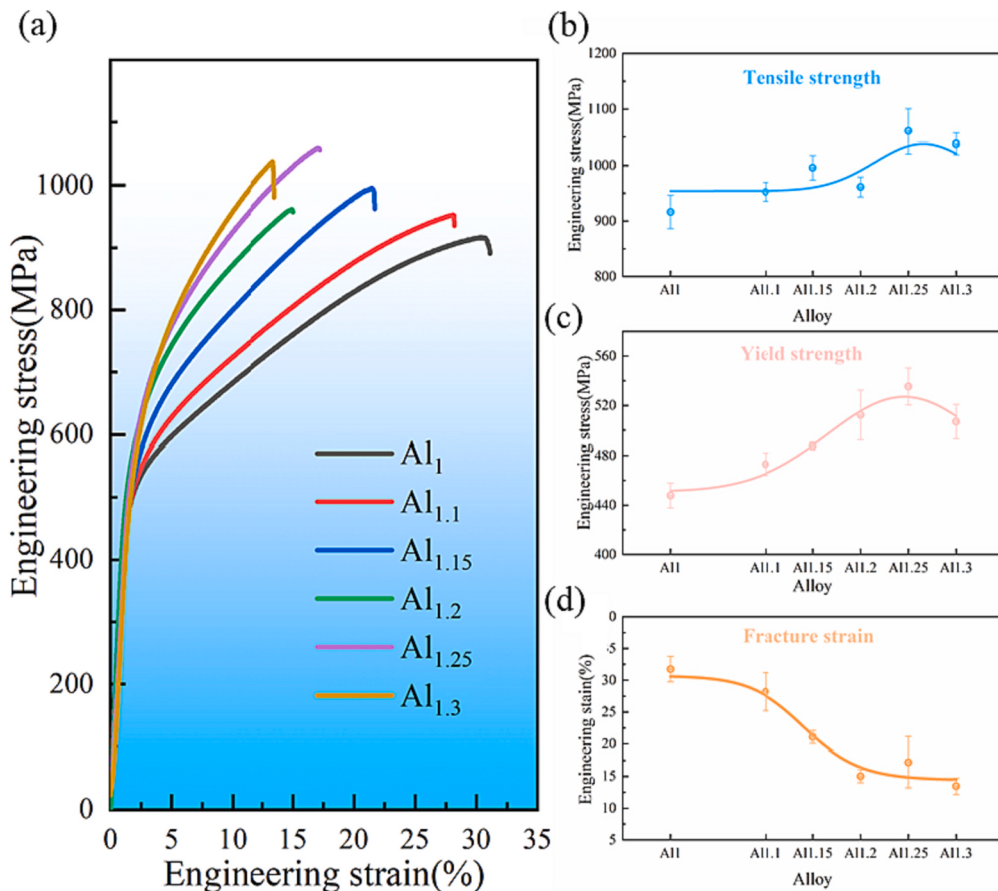


Fig. 4. Tensile mechanical properties of $\text{Al}_x\text{CoCrFeNi}_3$ HEAs: (a) Engineering stress-strain curve; (b) Tensile strength curve; (c) Yield strength curve; (d) Fracture strain curve.

Table 2
Tensile mechanical properties of $\text{Al}_x\text{CoCrFeNi}_3$ HEAs.

Alloy	Yield strength (MPa)	Tensile strength (MPa)	Fracture strain (%)
Al ₁	447.77	916.45	31.16
Al _{1.1}	473.03	952.64	28.20
Al _{1.15}	487.61	995.78	21.70
Al _{1.2}	512.34	961.18	15.01
Al _{1.25}	535.32	1060.59	17.21
Al _{1.3}	507.00	1038.37	13.46

the fracture morphologies have dimple and cleavage surface morphologies, so the fracture mode is ductile-brittle mixed quasi-cleavage fracture. The fracture of Al₁ alloy is mainly dimple morphology, which is due to the high proportion of soft FCC phase, resulting in excellent plasticity. With the increase of Al content, the proportion of eutectic lamellar structure increases, and the fracture morphology of the lamellar shape is formed.

(a) Al₁ alloy; (b) Al_{1.1} alloy; (c) Al_{1.15} alloy; (d) Al_{1.2} alloy; (e) Al_{1.25} alloy; (f) Al_{1.3} alloy.

4. Discussions

4.1. Strengthening Mechanism

In this work, Al_{1.25} alloy achieves a balance between strength and plasticity. This excellent strength and plasticity are mainly attributed to the fine eutectic lamellar structure. The alternating soft FCC and hard BCC eutectic structure can not only maintain the plasticity but also improve the strength. The main strengthening mechanism is the phase

interfacial strengthening mechanism. In addition, grain boundary strengthening, solid solution strengthening and friction stress strengthening are also important strengthening mechanisms. These strengthening mechanisms mainly hinder the movement of dislocations by increasing lattice distortion, generating phase interfaces and generating hard second phases, thereby jointly improving the strength of the alloy. For further calculation, the nanoindentation test was carried out on Al_{1.25} alloy. The nanoindentation morphology and parameters of BCC and FCC phases are shown in Fig. 7. The elastic modulus of FCC phase and BCC phase are 127.43 GPa and 232.27 GPa, respectively.

According to the continuum dislocation pile-up theory, the strengthening of heterogeneous interfaces consists of two main mechanisms: Interface independent barrier strength determined by the Hall-Petch formula (τ_a) and strengthening caused by modulus mismatch (τ_K) [47]. The overall interface barrier strength (τ_{int}) can be expressed as,

$$\tau_{int} = \tau_a + \tau_K \quad (1)$$

τ_a can be expressed as,

$$\tau_a = \frac{\pi k^2}{Gb(1-\nu)} \quad (2)$$

where k is the Hall-Petch constant that relates the interfacial yield strength to the dislocation stacking length, b is Poisson vector and ν is Poisson's ratio, estimated as 0.145 MPa·m^{0.5}, 0.148 nm and 0.3, respectively [48]. G is shear modulus, which can be obtained from the nanoindentation test results and the relationship between the elastic modulus and the shear modulus $G = \frac{E}{2(1+\nu)}$. τ_a is calculated to be 7.14 GPa.

τ_K is the Koehler stresses caused by the modulus mismatch, which

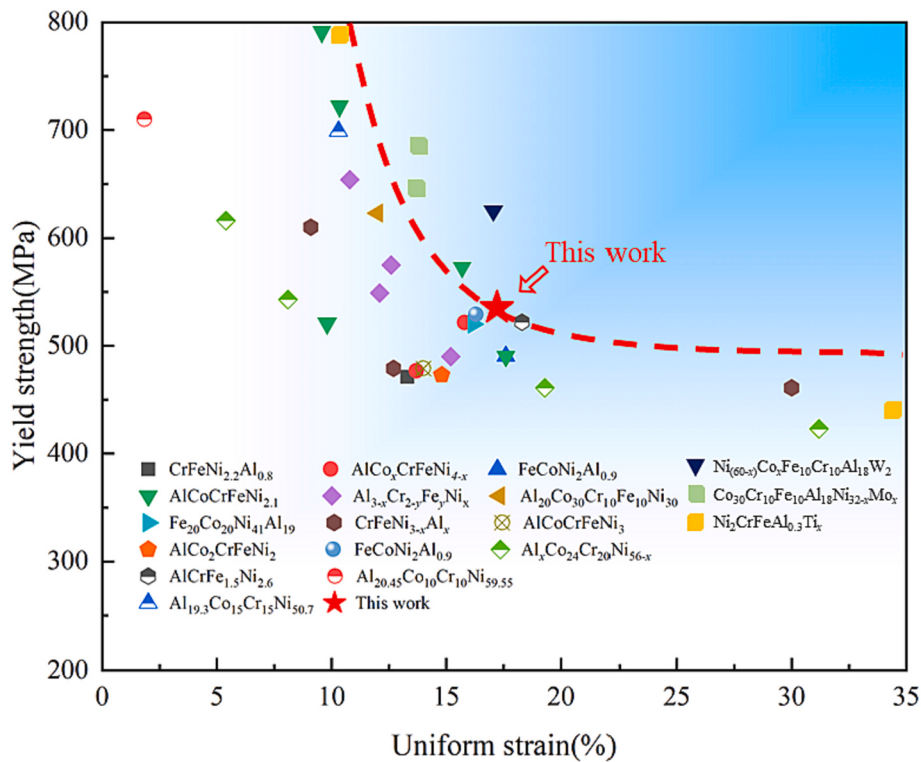


Fig. 5. Comparison of yield strength and uniform strain of Al_{1.25} alloy and other eutectic and near-eutectic AlCoCrFeNi HEAs [18,19,22,29–46].

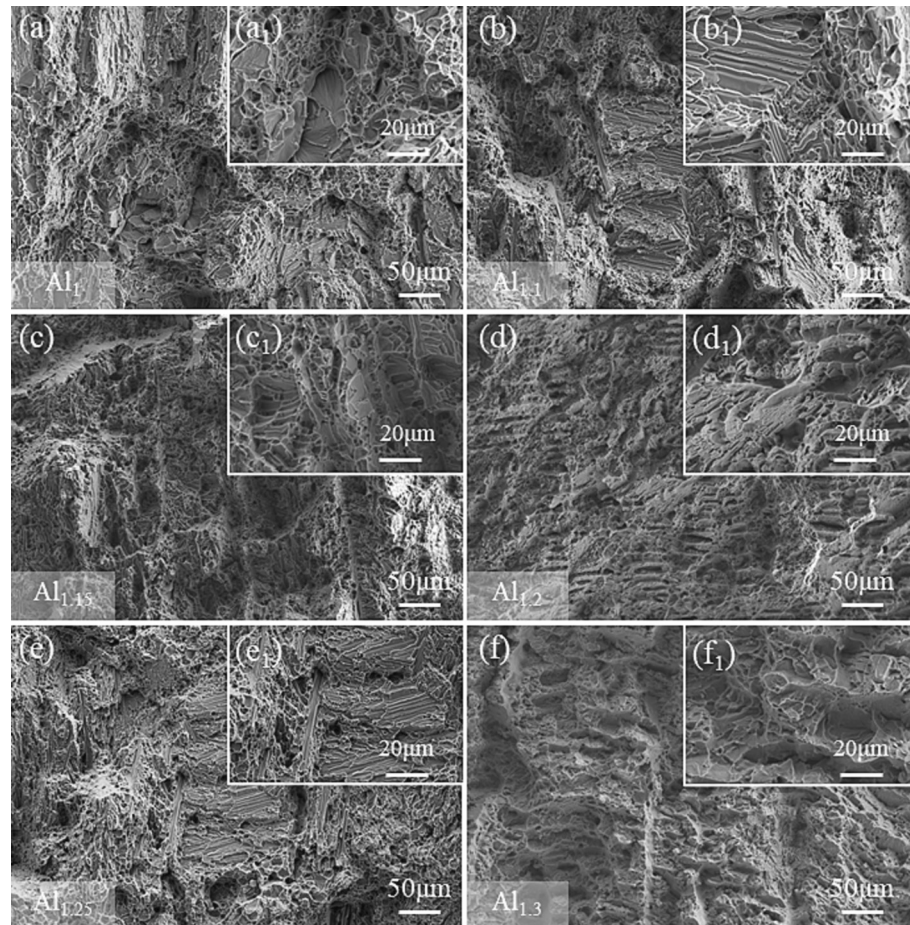


Fig. 6. Fracture micrographs of Al_xCoCrFeNi₃ HEAs:

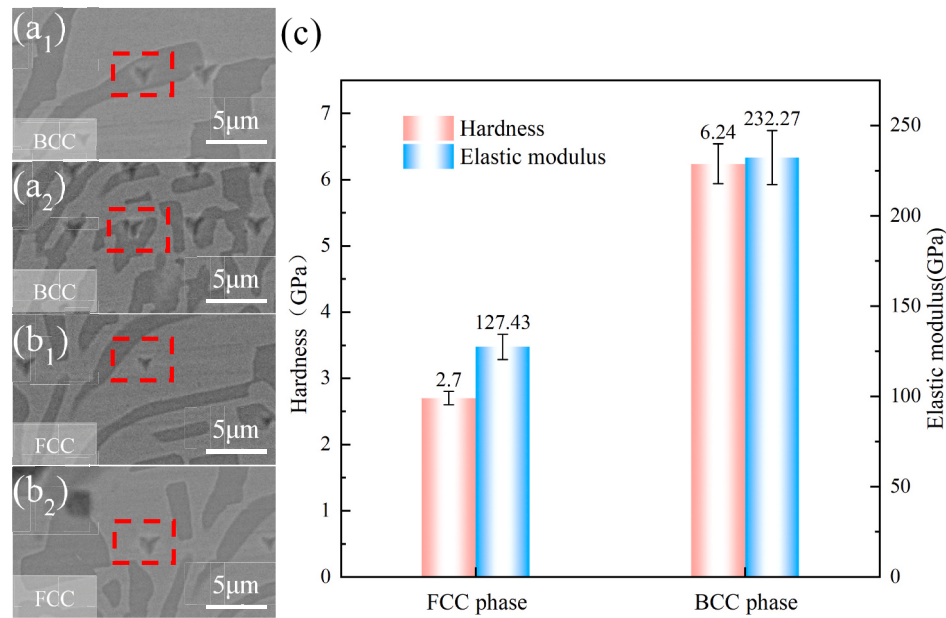


Fig. 7. Diagram of nanoindentation and parameters: (a) BCC phase nanoindentation diagram; (b) FCC phase nanoindentation diagram; (c) Hardness and modulus of elasticity parameters.

can be expressed as [49],

$$\tau_K = \frac{(G_{BCC} - G_{FCC})}{4\pi(G_{BCC} + G_{FCC})} \cdot \frac{G_{FCC}}{2} \quad (3)$$

where G_{FCC} and G_{BCC} are the shear modulus of FCC and BCC phases respectively. Here, the estimated τ_K is 0.61 GPa. In summary, the overall interfacial barrier strength (τ_{int}) is 7.75 GPa. According to dislocation pile-up theory, the heterogeneous interfacial strengthening ($\Delta\sigma_{int}$) is related to the strength of the interfacial barrier strength (τ_{int}), given as [50],

$$\Delta\sigma_{int} = \left[\frac{Gb\tau_{int}}{\pi(1-\nu)} \right]^{\frac{1}{2}} \bullet L^{-\frac{1}{2}} \quad (4)$$

where, L is the pile-up length (estimated as the thickness of lamellar FCC phase, 1 μm). Therefore, the contribution of interfacial strengthening to yield strength is calculated to be 209.4 MPa.

In addition to the above interface strengthening mechanism, grain boundary ($\Delta\sigma_G$) strengthening, solid solution strengthening ($\Delta\sigma_S$) and

friction strengthening (σ_0) are also important strengthening mechanisms. In order to further calculate the strengthening value, EBSD analysis was conducted on the microstructure, and the experimental results are shown in Fig. 8. It can be seen from the IPF diagram (Fig. 8 (a)) that the width of the grains is about 40 μm. It can be seen from the phase diagram (Fig. 8(b)) that the proportion of FCC phase is about 58%, and the proportion of BCC phase is about 42%. Grain boundary strengthening ($\Delta\sigma_G$) can be calculated according to the Hall-Petch formula [51]:

$$\Delta\sigma_{gb} = kd^{-\frac{1}{2}} \quad (5)$$

where k is the strengthening factor (estimated to be 667 MPa·μm^{1/2} [52]) and d is the grain diameter. After calculation, the grain boundary strengthening is 105.46 MPa.

Due to the small difference in mixing enthalpy and elemental radii between Co, Cr, Fe and Ni, Al_{1.25}CoCrFeNi₃ can be regarded as Co-Cr-Fe-Ni as solvent and Al with large atomic radii as solute. Due to the different content of Al in FCC phase and BCC phase, the solid solution strengthening can be calculated according to the mixed formula [53]:

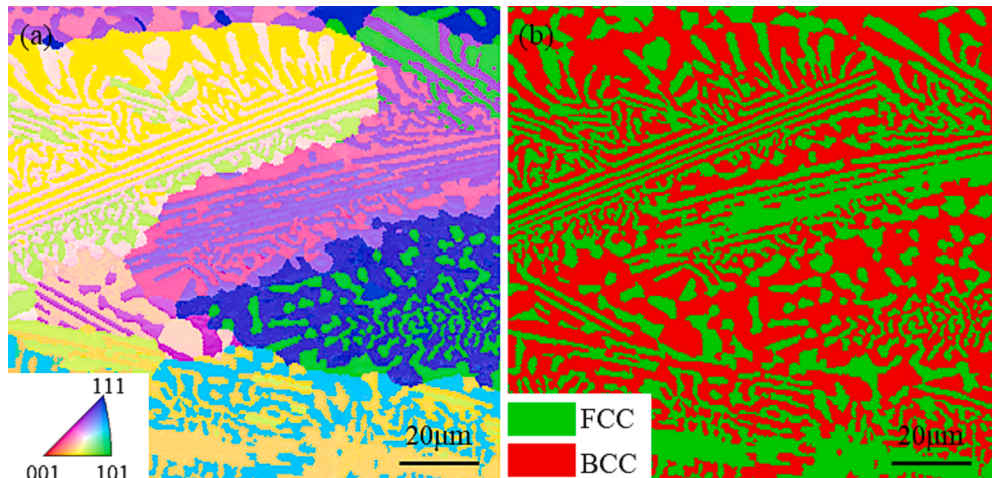


Fig. 8. EBSD pattern of microstructure: (a) Grain distribution; (b) Phase diagram.

$$\Delta\sigma_s = V_{FCC}\Delta\sigma_{SFCC} + V_{BCC}\Delta\sigma_{SBCC} \quad (6)$$

where V_{FCC} and V_{BCC} represent the volume fraction of the two phases, respectively. $\Delta\sigma_{SFCC}$ and $\Delta\sigma_{SBCC}$ represent the strengthening values of FCC phase and BCC phase, respectively. The displacement solid solution strengthening model based on dislocation-solute interaction represents solid solution strengthening, and the expression is [54],

$$\Delta\sigma_s = M \cdot \frac{G \cdot \varepsilon_s^{3/2} \cdot c^{1/2}}{700} \quad (7)$$

where M is the Taylor factor (3.06 for both FCC and BCC). G is the shear modulus, which can be calculated according to $G = \frac{E}{2(1+\nu)}$, and c is the atomic ratio of Al.

Interaction parameter ε_s can be expressed as,

$$\varepsilon_s = \left| \frac{\varepsilon_G}{1 + 0.5\varepsilon_G} - 3\varepsilon_a \right| \quad (8)$$

Based on the relationship between elasticity and atomic size mismatch, the relationship between ε_G and ε_a can be expressed as

$$\varepsilon_G = \frac{1}{G} \frac{\partial G}{\partial c} \quad (9)$$

$$\varepsilon_a = \frac{1}{a} \frac{\partial a}{\partial c} \quad (10)$$

The parameter ε_G can be neglected compared with ε_a , a is the lattice parameter, which can be obtained by XRD patterns. The lattice parameters of FCC phase and BCC phase are 0.35818 nm and 0.28685 nm, respectively. The solid solution strengthening ($\Delta\sigma_s$) value is calculated to be 127.82 MPa.

The friction stress strengthening (σ_0) caused by lattice friction also improves the yield strength. Since σ_0 depends on the lattice, the friction stress strengthening can be estimated by the mixing rule [55]. The formula is expressed as,

$$\sigma_0 = \sum_{i=1}^n c_i \sigma_i \quad (11)$$

where σ_i represents the lattice friction stress of a single element, and the data are shown in Table 3. The friction stress strengthening (σ_0) is calculated to be 89.73 MPa.

According to the above calculation and discussion, the theoretical calculation value of yield strength (σ_y) is $\sigma_y = \sigma_0 + \Delta\sigma_G + \Delta\sigma_s + \Delta\sigma_{int} = 532.41$ MPa. In order to facilitate the comparison between the calculated data and the experimental data and to clearly compare the contribution values of various strengthening mechanisms, a histogram is drawn, as shown in Fig. 9. Obviously, the calculated data are in good agreement with the experimental data, and the phase interface strengthening contributes the most to the improvement of strength. The errors in the calculation results are mainly due to the calculation model and the parameter references to conventional alloys. Nevertheless, the agreement between the calculated and experimental data is very satisfactory.

4.2. Deformation Behavior

In order to better understand the micromechanical behavior of heterogeneous dual-phase eutectic Al_{1.25} alloy and establish the relationship between mechanical properties and microstructure, the microscopic deformation behavior and crack initiation mechanism

Table 3

Lattice friction of each element in the HEA cladding layers [55].

Element	Al	Co	Cr	Fe	Ni
σ_i (MPa)	16	10.3	454	100	22

during the tensile process are further discussed.

The heterogeneous eutectic Al_{1.25} alloy has a soft and hard alternating BCC/FCC lamellar structure (as shown in Figs. 2 and 7). During tensile deformation, the soft FCC phase is more prone to plastic deformation. However, FCC phase is rigidly constrained by the hard BCC lamellar phase and cannot undergo significant plastic deformation. According to the principle of strain continuity, a plastic strain gradient is generated in the FCC phase near the BCC-FCC interface and geometrically necessary dislocations (GNDs) are stored [56,57]. Therefore, under the constraint of BCC phase, a long-range back stress is generated near the heterogeneous interface in the FCC phase, making it difficult to move dislocations in the FCC phase [58,59]. FCC phase exhibits higher strength than the unconstrained phase, forming a synergistic strengthening effect and further increasing the strength [60].

In order to further explore the deformation and fracture mechanism of Al_{1.25} alloy, strain analysis and microscopic crack observation are carried out on the microstructure of the fracture sample, as shown in Fig. 10. High Kernel average misorientation (KAM) values can be observed at the phase interface (Fig. 10(b)), and dislocations accumulate significantly at the BCC-FCC interface. Obvious strain can also be seen in BCC phase (as shown in Fig. 10(b)). It is worth noting that the KAM value of BCC phase in the irregular eutectic region is higher than that in the regular eutectic region, indicating that BCC phase in the irregular eutectic region has more severe strain. Fig. 10(d) shows that the crack is formed in the BCC phase rather than at the FCC-BCC interface. Some cracks stop expanding within BCC phase, and some cracks penetrate BCC phase and are stopped as they enter FCC phase. When the crack enters FCC phase, the crack tip undergoes significant passivation due to the inherent crack-tip blunting and crack-tip plasticity mechanisms [30], making it difficult to expand in the FCC phase and delaying the fracture.

Based on the above discussion of deformation and fracture, a schematic diagram of micromechanical behavior and microstructural evolution in the tensile deformation process is drawn. As shown in Fig. 11, the tensile process is divided into four stages. In the first stage of stretching, FCC phase exhibits an earlier yielding due to the relatively low strength, resulting in the creation of statistically stored dislocations (SSDs) in FCC, as shown in Fig. 11(a). There is continuous strain hardening in FCC phase due to the rigid constraint of the hard BCC lamellar phase. In the second stage (Fig. 11(b)), as the tensile process proceeds, FCC phase continues to undergo plastic deformation, while the hard BCC phase continues to undergo elastic deformation, resulting in strain incompatibility between FCC phase and BCC phase. According to the strain gradient plasticity theory, GNDs will be generated near the BCC-FCC interface. Since the soft FCC phase is constrained by the adjacent hard BCC phase, GNDs will accumulate at the phase interface and generate back stress in the FCC phase (represented by green arrows in Fig. 11(b)) and forward stress in the BCC phase (represented by blue arrows in Fig. 11(b)) [61]. The formation of forward stress makes the stress transfer from the soft FCC phase to BCC phase, which reduces the stress in FCC phase and improves the strength of the alloy. In the third stage of tension, the strain incompatibility between the two phases increases and the dislocation accumulation becomes more serious. The stress continues to transfer from FCC phase to BCC phase, eventually leading to the formation of a crack in the BCC phase near the interface. In the fourth stage (Fig. 11(d)), as the stretching process progresses, the crack gradually expands and penetrates the BCC phase. When the crack enters FCC phase, obvious passivation occurs at the crack tip due to the limitation of the ductile FCC phase, so that the residual intergranular/intragranular strain hardening ability can last longer and delay the further propagation of the crack, thus maintaining the strength and plasticity. Further increasing the tensile stress, the cracks gradually bridge and eventually lead to the failure of the sample.

5. Conclusions

In this work, the effect of Al content on the microstructure and

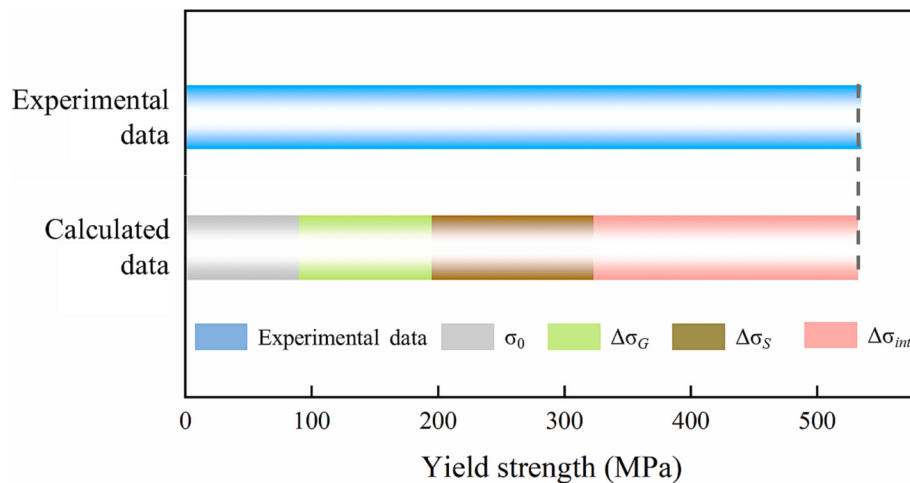


Fig. 9. Comparison of experimental data and calculated data.

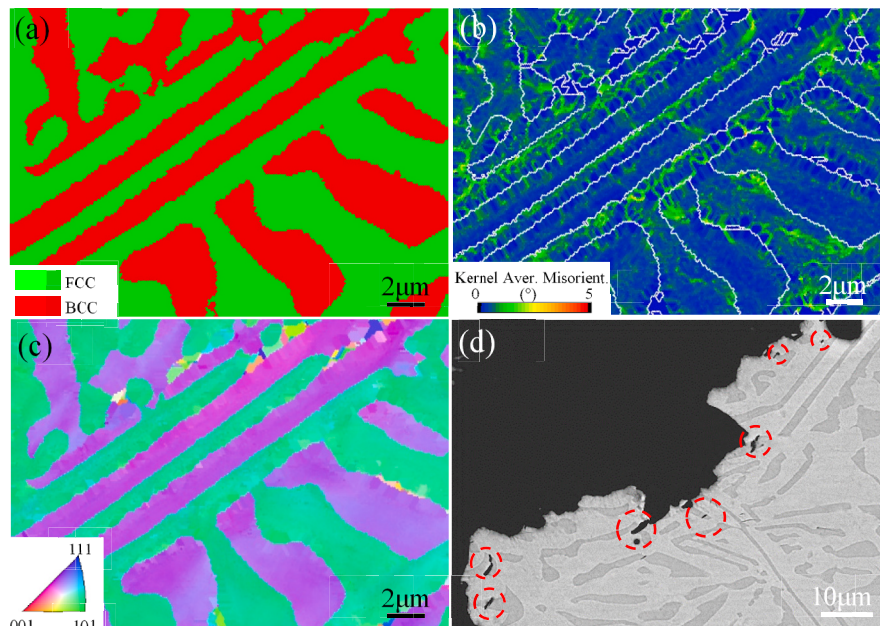


Fig. 10. Schematic diagram of strain distribution and crack extension of fractured $\text{Al}_{1.25}$ alloy: (a) EBSD phase map; (b) KAM map; (c) Inverse pole figure; (d) Microcrack morphology.

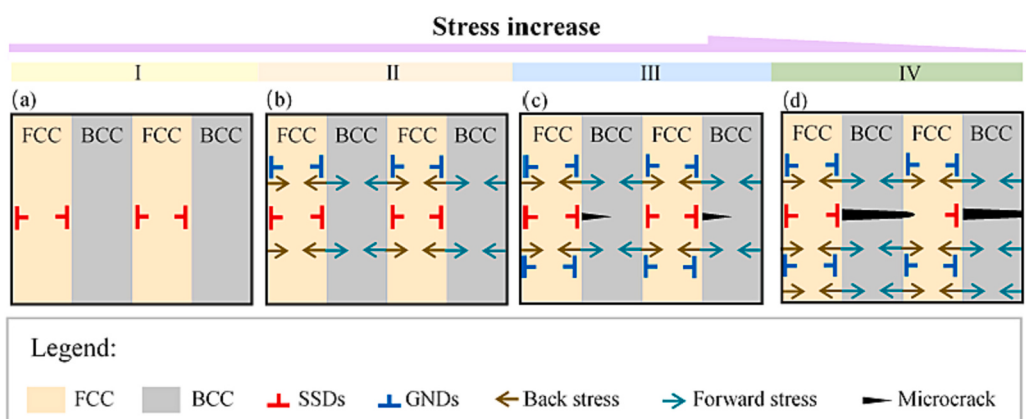


Fig. 11. Schematic diagrams of the microstructure evolution and micromechanical behavior during tensile deformation: (a) First stage; (b) Second stage; (c) Third stage; (d) Fourth stage.

mechanical properties of $\text{Al}_x\text{CoCrFeNi}_3$ HEAs is systematically studied. The strengthening mechanism and deformation behavior of $\text{Al}_{1.25}\text{CoCrFeNi}_3$ alloy are emphatically analyzed, and the relationship between microstructure evolution and micromechanical behavior is established. The main conclusions are as follows:

- (1) With the increase of Al, $\text{Al}_x\text{CoCrFeNi}_3$ HEAs gradually change from hypoeutectic structure to hypereutectic structure. $\text{Al}_{1.25}\text{CoCrFeNi}_3$ alloy exhibits a fine FCC/BCC eutectic lamellar structure.
- (2) The yield strength of $\text{Al}_x\text{CoCrFeNi}_3$ HEAs increases first and then decreases with the increase of Al, and the plasticity keeps decreasing. $\text{Al}_{1.25}\text{CoCrFeNi}_3$ HEA has the highest yield strength, tensile strength and good plasticity, which are 535.32 MPa, 1060.59 MPa and 17.21%, respectively, showing a good balance of strength and plasticity.
- (3) Interfacial strengthening, grain boundary strengthening, solid solution strengthening and friction stress strengthening are the main strengthening mechanisms of $\text{Al}_{1.25}\text{CoCrFeNi}_3$ HEA, in which BCC-FCC interfacial strengthening plays a major role. The theoretical calculation values are in good agreement with the experimental data.
- (4) During the tensile process, the fine eutectic lamellar heterostructure inhibits the plastic deformation of FCC and forms a back stress, resulting in strain hardening and synergistic strengthening. The generation of back and forward stresses leads to a continuous transfer of stress from FCC phase to BCC phase, resulting in the initiation and propagation of cracks in the BCC phase.

CRediT authorship contribution statement

Xu Yang: Conceptualization, Data curation, Writing – original draft. **Li Feng:** Writing – review & editing. **Tong Liu:** Writing – review & editing. **Ruirun Chen:** Project administration, Supervision, Investigation, Funding acquisition, Conceptualization. **Gang Qin:** Writing – review & editing. **Shiping Wu:** Validation.

Declaration of Competing Interest

The authors declare that they have no known competing financial interests or personal relationships that could have appeared to influence the work reported in this paper.

Data availability

The authors do not have permission to share data.

Acknowledgements

This work was supported by the National Natural Science Foundation of China (No. 51825401) and Interdisciplinary Research Foundation of HIT.

References

- [1] J.W. Yeh, S.K. Chen, S.J. Lin, J.Y. Gan, T.S. Chin, T.T. Shun, C.H. Tsau, S.Y. Chang, Nanostructured high-entropy alloys with multiple principal elements: novel alloy design concepts and outcomes, *Adv. Eng. Mater.* 6 (2004) 299–303.
- [2] B. Cantor, I.T.H. Chang, P. Knight, A.J.B. Vincent, Microstructural development in equiatomic multicomponent alloys, *Mater. Sci. Eng. A* 6 (2004) 213–218.
- [3] Q.Q. Ding, Y. Zhang, X. Chen, X.Q. Fu, D.K. Chen, S.J. Chen, L. Gu, F. Wei, H.B. Bei, Y.F. Gao, M.R. Wen, J.X. Li, Z. Zhang, T. Zhu, R.O. Ritchie, Q. Yu, Tuning element distribution, structure and properties by composition in high-entropy alloys, *Nature* 574 (2019) 223–227.
- [4] R.P. Zhang, S.T. Zhao, J. Ding, Y. Chong, T. Jia, C. Ophus, M. Asta, R.O. Ritchie, A. M. Minor, Short-range order and its impact on the CrCoNi medium-entropy alloy, *Nature* 581 (2020) 283–287.
- [5] Q.Q. Wei, Z.R. Liu, Q. Shen, J.H. Chen, X.D. Xu, Enhanced strength and plasticity in a $\text{Nb}_2\text{MoWC}0.5$ alloy via eutectic dilute carbide, *Mater. Sci. Eng. A* 872 (2023) 144920.
- [6] S.H. Shim, H. Pouraliakbar, H. Minouei, M.S. Rizi, V. Fallah, Y.S. Na, J.H. Han, S. I. Hong, Characterization of the microscale/nanoscale hierarchical microstructure of an as-cast CrMnFeNiCu high-entropy alloy with promising mechanical properties, *J. Alloys Compd.* 954 (2023) 170091.
- [7] S.H. Shim, H. Pouraliakbar, S.I. Hong, Hierarchical structured as-cast $\text{CrFeNiMn}_{0.5}\text{Cu}_{0.5}$ high entropy alloy with excellent tensile strength/ductility properties, *Scr. Mater.* 210 (2022) 114473.
- [8] C. Zhang, Q. Yu, Y.B.T. Tang, M.J. Xu, H.R. Wang, C.Y. Zhu, J. Ell, S.T. Zhao, B. E. MacDonald, P.H. Cao, J.M. Schoenung, K.S. Vecchio, R.C. Reed, R.O. Ritchie, E. J. Lavernia, Strong and ductile FeNiCoAl -based high-entropy alloys for cryogenic to elevated temperature multifunctional applications, *Acta Mater.* 242 (2023) 118449.
- [9] Z.Q. Xu, Z.L. Ma, Y. Tan, X.W. Cheng, Designing TiVNbTaSi refractory high-entropy alloys with ambient tensile ductility, *Scr. Mater.* 206 (2022) 114230.
- [10] T. Liu, R.R. Chen, X.F. Gao, H.Z. Fang, G. Qin, Y.Q. Su, J.J. Guo, Formation of hypoeutectic structure and strengthening mechanism of $\text{Co}_4\text{Cr}_{1.5}\text{Fe}_{1.5}\text{Ni}_5$ high entropy alloy alloyed by Al, *J. Alloys Compd.* 923 (2022) 166372.
- [11] S.H. Shim, H. Pouraliakbar, Y.K. Kim, B.J. Lee, V. Fallah, Y.K. Kim, K.R. Lim, Y. S. Na, S.I. Hong, Exploring the impact of heat treatment on the transformation of hierarchical microstructure and mechanical properties in a non-equiatomic CrMnFeNiCu high-entropy alloy with a reversible structure, *J. Alloys Compd.* 969 (2023) 172251.
- [12] H. Pouraliakbar, S.H. Shim, Y.K. Kim, M.S. Rizi, H. Noh, S.I. Hong, Microstructure evolution and mechanical properties of $(\text{CoCrNi})_{90}(\text{AlTiZr})_5(\text{CuFeMo})_5$ multicomponent alloy: a pathway through multicomponent alloys toward new superalloys, *J. Alloys Compd.* 8600 (2021) 158412.
- [13] X.F. Gao, R.R. Chen, T. Liu, H.Z. Fang, G. Qin, Y.Q. Su, J.J. Guo, High entropy alloys: a review of mechanical properties and deformation mechanisms at cryogenic temperatures, *J. Mater. Sci.* 57 (2022) 6573–6606.
- [14] E. Manta, M. Lucaci, E. Vasile, M.V. Lungu, D. Tăleanu, N. Stancu, A. Iorga, Influence of processing route on microstructure and properties of $\text{Al}_{13.45}\text{FeCrNiCo}$ high entropy alloys, *J. Alloys Compd.* 907 (2022) 164457.
- [15] L. Tang, L. Wang, M.S. Wang, H.B. Liu, S. Kabra, Y.L. Chiu, B. Cai, Synergistic deformation pathways in a TWIP steel at cryogenic temperatures: in situ neutron diffraction, *Acta Mater.* 200 (2020) 943–958.
- [16] C.S. Zheng, W.W. Yu, Effect of low-temperature on mechanical behavior for an AISI 304 austenitic stainless steel, *Mater. Sci. Eng. A* 710 (2018) 359–365.
- [17] Y.P. Lu, Y. Dong, S. Guo, L. Jiang, H.J. Kang, T.M. Wang, B. Wen, Z.J. Wang, J. C. Jie, Z.Q. Cao, H.H. Ruan, T.J. Li, A promising new class of high-temperature alloys: eutectic high-entropy alloys, *Sci. Rep.* 4 (2014) 6200.
- [18] P.J. Shi, R.G. Li, Y. Li, Y.B. Wen, Y.B. Zhong, W.L. Ren, Z. Shen, T.X. Zheng, J. C. Peng, X. Liang, P.F. Hu, N. Min, Y. Zhang, Y. Ren, P.K. Liaw, D. Raabe, Y. D. Wang, Hierarchical crack buffering triples ductility in eutectic herringbone high-entropy alloys, *Science* 373 (2021) 912–918.
- [19] Z.Z. Mao, X. Jin, Z. Xue, M. Zhang, J.W. Qiao, Understanding the yield strength difference in dual-phase eutectic high-entropy alloys, *Mater. Sci. Eng. A* 867 (2023) 144725.
- [20] Y. Lu, Y. Dong, H. Jiang, Z. Wang, Z. Cao, S. Guo, T. Wang, T. Li, P.K. Liaw, Promising properties and future trend of eutectic high entropy alloys, *Scr. Mater.* 187 (2020) 202–209.
- [21] C.S. Tiwary, P. Pandey, S. Sarkar, R. Das, S. Samal, K. Biswas, K. Chattopadhyay, Five decades of research on the development of eutectic as engineering materials, *Prog. Mater. Sci.* 123 (2021) 100793.
- [22] B. Chanda, G. Potnis, P.P. Jana, J. Das, A review on nano-/ultrafine advanced eutectic alloys, *J. Alloys Compd.* 827 (2020) 154226.
- [23] L. Wang, C.L. Yao, J. Shen, Y.P. Zhang, T. Wang, Y.H. Ge, L.H. Gao, G.J. Zhang, Microstructures and room temperature tensile properties of as-cast and directionally solidified $\text{AlCoCrFeNi}_{2.1}$ eutectic high-entropy alloy, *Intermetallics* 118 (2020), 106681.
- [24] L. Wang, X.Y. Wu, C.L. Yao, J. Shen, Y.P. Zhang, Y.H. Ge, G.J. Zhang, Microstructural stability of as-cast and directionally solidified $\text{AlCoCrFeNi}_{2.1}$ eutectic high-entropy alloys at elevated temperatures, *Metall. Mater. Trans. A* 51 (2020) 5781–5789.
- [25] M.L. Wang, Y.P. Lu, J.G. Lan, T.M. Wang, C. Zhang, Z.Q. Cao, T.J. Li, P.K. Liaw, Lightweight, ultrastrong and high thermal-stable eutectic high-entropy alloys for elevated-temperature applications, *Acta Mater.* 248 (2023) 118806.
- [26] X.C. Ye, J.Y. Xiong, X. Wu, C. Liu, D. Xu, W. Zhang, D. Fang, B. Li, A new infinite solid solution strategy to design eutectic high entropy alloys with B2 and BCC structure, *Scr. Mater.* 199 (2021) 113886.
- [27] Q.F. Wu, Z.J. Wang, X.B. Hu, T. Zheng, Z.S. Yang, F. He, J.J. Li, J.C. Wang, Uncovering the eutectics design by machine learning in the $\text{Al}-\text{co}-\text{Cr}-\text{Fe}-\text{Ni}$ high entropy system, *Acta Mater.* 182 (2020) 278–286.
- [28] Q.F. Wu, Z.J. Wang, F. He, Y.F. Wei, J.J. Li, J.C. Wang, Rapid alloy design from superior eutectic high-entropy alloys, *Scr. Mater.* 219 (2022) 114875.
- [29] P.J. Shi, Y.B. Zhong, B. Yan, J.C. Peng, P.F. Hu, Y. Zhang, P.K. Liaw, Y.T. Zhu, Multistage work hardening assisted by multi-type twinning in ultrafine-grained heterostructural eutectic high-entropy alloys, *Mater. Today* 41 (2020) 62–71.
- [30] D.H. Chung, J. Lee, Q.F. He, Y.K. Kim, K.R. Lim, H.S. Kim, Y. Yang, Y.S. Na, Hetero-deformation promoted strengthening and toughening in BCC rich eutectic and near eutectic high entropy alloys, *J. Mater. Sci. Technol.* 146 (2023) 1–9.
- [31] Q.F. Wu, Z.J. Wang, T. Zheng, D. Chen, Z.S. Yang, J.J. Li, J.J. Kai, J.C. Wang, A casting eutectic high entropy alloy with superior strength-ductility combination, *Mater. Lett.* 253 (2019) 268–271.

- [32] Z.S. Yang, Z.J. Wang, Q.F. Wu, T. Zheng, P.R. Zhao, J.K. Zhao, J.Y. Chen, Enhancing the mechanical properties of casting eutectic high entropy alloys with Mo addition, *Appl. Phys. A Mater. Sci. Process.* 125 (2019) 208.
- [33] Q.F. Wu, F. He, J.J. Li, H.S. Kim, Z.J. Wang, J.C. Wang, Phase-selective recrystallization makes eutectic high-entropy alloys ultra-ductile, *Nat. Commun.* 13 (2022) 4697.
- [34] Y. Dong, Z.Q. Yao, X. Huang, F.M. Du, C.Q. Li, A.F. Chen, F. Wu, Y.Q. Cheng, Z. R. Zhang, Microstructure and mechanical properties of Al_{Co_x}CrFeNi_{3-x} eutectic high-entropy-alloy system, *J. Alloys Compd.* 823 (2020) 153886.
- [35] Y. He, M.P. Lei, W.H. Ma, R.L. Zhang, Y. Lei, A new approach to determine/design the eutectic composition of binary, ternary, and high-entropy alloys using electromagnetic directional crystallization, *J. Alloys Compd.* 916 (2022) 165410.
- [36] Q.W. Tian, G.J. Zhang, K.X. Yin, W.L. Cheng, Y.N. Wang, J.C. Huang, Effect of Ni content on the phase formation, tensile properties and deformation mechanisms of the Ni-rich Al_{CoCrFeNi_x} ($x=2, 3, 4$) high entropy alloys, *Mater. Charact.* 176 (2021) 111148.
- [37] Y.P. Lu, X.Z. Gao, L. Jiang, Z.N. Chen, T.M. Wang, J.C. Jie, H.J. Kang, Y.B. Zhang, S. Guo, H.H. Ruan, Y.H. Zhao, Z.Q. Cao, T.J. Li, Directly cast bulk eutectic and near-eutectic high entropy alloys with balanced strength and ductility in a wide temperature range, *Acta Mater.* 124 (2017) 143–150.
- [38] X. Jin, J. Bi, L. Zhang, Y. Zhou, X.Y. Du, Y.X. Liang, B.S. Li, A new CrFeNi_{2Al} eutectic high entropy alloy system with excellent mechanical properties, *J. Alloys Compd.* 770 (2019) 655–661.
- [39] X. Jin, Y. Zhou, L. Zhang, X.Y. Du, B.S. Li, A new pseudo binary strategy to design eutectic high entropy alloys using mixing enthalpy and valence electron concentration, *Mater. Des.* 143 (2018) 49–55.
- [40] X. Wang, W. Zhai, J.Y. Wang, B. Wei, Strength and ductility enhancement of high-entropy FeCoNi_{2Al_{0.9}} alloy by ultrasonically refining eutectic structures, *Scr. Mater.* 225 (2023) 115154.
- [41] L.L. Ma, J.N. Wang, Z.H. Lai, Z.C. Wu, B.T. Yang, P.P. Zhao, Microstructure and mechanical property of Al_{56-x}Co₂₄Cr₂₀Ni_x eutectic high-entropy alloys with an ordered FCC/BCT phase structure, *J. Alloys Compd.* 936 (2023) 168194.
- [42] H. Wu, J. Xie, H.Y. Yang, D.L. Shu, G.C. Hou, J.G. Li, Y.Z. Zhou, X.F. Sun, A cost-effective eutectic high entropy alloy with an excellent strength-ductility combination designed by VEC criterion, *J. Mater. Res. Technol.* 19 (2022) 1759–1765.
- [43] Q.Q. Liu, X.S. Liu, X.F. Fan, R. Liu, X. Tong, P.F. Yu, G. Li, Designing novel Al_{CoCrNi} eutectic high entropy alloys, *J. Alloys Compd.* 904 (2022) 163775.
- [44] X.S. Chen, J. Kong, J.L. Li, S. Feng, H. Li, Q.P. Wang, Y.Z. Liang, K.W. Dong, Y. Yang, High-strength Al_{CoCrFeNi_{2.1}} eutectic high entropy alloy with ultrafine lamella structure via additive manufacturing, *Mater. Sci. Eng. A* 854 (2022) 143816.
- [45] L.F. Huang, Y.N. Sun, N. Chen, H.W. Luan, G.M. Le, X. Liu, Y.Q. Ji, Y.P. Lu, P. K. Liaw, X.S. Yang, Y.Z. Zhou, J.F. Li, Simultaneously enhanced strength-ductility of AlCoCrFeNi_{2.1} eutectic high-entropy alloy via additive manufacturing, *Mater. Sci. Eng. A* 830 (2022) 142327.
- [46] X.X. Liu, S.G. Ma, W.D. Song, D. Zhao, Z.H. Wang, Microstructure evolution and mechanical response of co-free Ni₂CrFeAl_{0.3}Tix high-entropy alloys, *J. Alloys Compd.* 931 (2023) 167523.
- [47] I. Basu, V. Ocelík, J. ThM. D. Hossen, BCC-FCC interfacial effects on plasticity and strengthening mechanisms in high entropy alloys, *Acta Mater.* 157 (2018) 83–95.
- [48] L.L. Liu, P. Shen, X.Z. Wu, R. Wang, W.G. Li, Q. Liu, First-principles calculations on the stacking fault energy, surface energy and dislocation properties of NbCr₂ and HfCr₂, *Comput. Mater. Sci.* 140 (2017) 334–343.
- [49] S.I. Rao, P.M. Hazzledine, Atomistic simulations of dislocation-interface interactions in the Cu-Ni multilayer system, *Philosophical* 80 (2000) 2011–2040.
- [50] Y.P. Cai, G.J. Wang, Y.J. Ma, Z.H. Cao, X.K. Meng, High hardness dual-phase high entropy alloy thin films produced by interface alloying, *Scr. Mater.* 162 (2019) 281–285.
- [51] W.H. Liu, Y. Wu, J.Y. He, T.G. Nieh, Z.P. Lu, Grain growth and the Hall-Petch relationship in a high-entropy FeCrNiCoMn alloy, *Scr. Mater.* 68 (2013) 526–529.
- [52] D. Wu, Junyan Zhang, J.C. Huang, H. Beid, T.G. Nieh, Grain-boundary strengthening in nanocrystalline chromium and the Hall-Petch coefficient of body-centered cubic metals, *Scr. Mater.* 68 (2013) 118–121.
- [53] X. Jin, Y.X. Liang, J. Bi, B.S. Li, Enhanced strength and ductility of Al_{0.9}CoCrNi_{2.1} eutectic high entropy alloy by thermomechanical processing, *Materialia* 10 (2020) 100639.
- [54] J.Y. He, H. Wang, H.L. Huang, X.D. Xu, M.W. Chen, Y. Wu, X.J. Liu, T.G. Nieh, K. An, Z.P. Lu, A precipitation-hardened high-entropy alloy with outstanding tensile properties, *Acta Mater.* 102 (2016) 187–196.
- [55] R. Sriharitha, B.S. Murty, R.S. Kottada, Alloying, thermal stability and strengthening in spark plasma sintered Al_xCoCrCuFeNi high entropy alloys, *J. Alloys Compd.* 583 (2014) 419–426.
- [56] C.X. Huang, Y.F. Wang, X.L. Ma, S. Yin, H.W. Höppel, M. Göken, X.L. Wu, H.J. Gao, Y.T. Zhu, Interface affected zone for optimal strength and ductility in heterogeneous laminate, *Mater. Today* 21 (2018) 713–719.
- [57] Y.T. Zhu, X.L. Wu, Perspective on hetero-deformation induced (HDI) hardening and back stress, *Mater. Res. Lett.* 7 (2019) 393–398.
- [58] L.J. Wang, L. Wang, S.C. Zhou, Q. Xiao, Y. Xiao, X.T. Wang, T.Q. Cao, Y. Ren, Y. J. Liang, L. Wang, Y.F. Xue, Precipitation and micromechanical behavior of the coherent ordered nanoprecipitation strengthened Al-Cr-Fe-Ni-V high entropy alloy, *Acta Mater.* 216 (2021) 117121.
- [59] K. Lu, Making strong nanomaterials ductile with gradients, *Science* 345 (2014) 6203.
- [60] M.X. Yang, Y. Pan, F.P. Yuan, Y.T. Zhu, X.L. Wu, Back stress strengthening and strain hardening in gradient structure, *Mater. Res. Lett.* 4 (2016) 145–151.
- [61] Y.F. Wang, C.X. Huang, X.T. Fang, H.W. Höppel, M. Göken, Y.T. Zhu, Hetero-deformation induced (HDI) hardening does not increase linearly with strain gradient, *Scr. Mater.* 174 (2020) 19–23.